RSC Advances

ROYAL SOCIETY OF CHEMISTRY

PAPER

View Article Online
View Journal | View Issue

Cite this: *RSC Adv.*, 2026, **16**, 20015

Field-free control of magnetism and electronic states in ZGNR/h-BN heterojunctions *via* topological line defects

Guochao Shan, Wenqiang Chen and Wei Liu *

The pursuit of fully spin-polarized currents remains a central challenge in spintronics. Zigzag graphene nanoribbon/hexagonal boron nitride (ZGNR/h-BN) heterojunctions offer a promising platform due to their stabilized edge states and tunable electronic properties. However, their inherent antiferromagnetic (AFM) order and limited means of external-field-free control hinder practical applications. Here, we demonstrate a deterministic strategy to achieve field-free manipulation of both magnetic order and electronic phases in ZGNR/h-BN heterojunctions by embedding pentagon-octagon (558) topological line defects. Density functional theory calculations reveal that this defect engineering spontaneously drives a transition from the pristine AFM state to a ferrimagnetic (FiM) ground state, originating from spin polarization reconstruction at the defect sites and asymmetric edge moments. Furthermore, the electronic properties exhibit programmable phase transitions: the system evolves from a conventional half-metal to a Dirac half-semimetal with Fermi velocities up to 3×10^5 m s^{-1}, and eventually to a full metal, as the ZGNR width increases. Remarkably, shifting the defect position enables continuous modulation of the spin-down bandgap (0–0.18 eV) and can even induce a ferromagnetic state. The FiM order and half-metallicity are robust under biaxial strain within ±5%, while a transition to ferromagnetism can be triggered by specific uniaxial strains. This work establishes a versatile pathway, integrating defect engineering with heterojunction design, for the on-demand, external-field-free control of spin and charge degrees of freedom in carbon-based nanostructures, paving the way for low-power spintronic devices.

Received 17th February 2026
Accepted 12th April 2026

DOI: 10.1039/d6ra01402j

rsc.li/rsc-advances

1. Introduction

Spintronics offers significant advantages over conventional charge-based electronics for information storage and processing, yet the critical challenge remains in designing novel materials exhibiting controllable spin polarization, long spin relaxation times, and high charge carrier mobility.[1–5] Zigzag graphene nanoribbons (ZGNRs), a graphene derivative, have emerged as ideal candidates for spintronic devices due to their tunable bandgaps and magnetically ordered ground state.[6–9] Nevertheless, pristine ZGNRs suffer from edge state instability induced by environmental perturbations, such as adsorbates and edge reconstruction.[10–12] Furthermore, their inherent antiferromagnetic (AFM) configuration results in zero net magnetic moment, hindering efficient spin injection and detection.[13] Embedding ZGNRs within wide-bandgap, atomically flat, and chemically inert two-dimensional (2D) h-BN to form heterojunctions provides a robust strategy for stabilizing edge states and modulating electronic properties. Such heterostructures have been successfully synthesized experimentally[13,14] and are theoretically predicted to simultaneously exhibit robust half-semimetallic behavior.[14–17] It is noteworthy, however, that these systems intrinsically maintain AFM ordering. Charge doping within these heterojunctions can induce a phase transition from AFM to ferrimagnetic (FiM) ordering, thereby enabling tunable spin-dependent functionalities.[14,18]

The precise introduction of topological defects serves as a critical strategy for modulating the electronic structures and magnetic properties of graphene-based materials.[19–23] Such defects can induce localized states, alter carrier types, and can even activate magnetic moments.[24–28] Among these defects, the pentagon-pentagon-octagon (558) topological line defect has been successfully synthesized in ZGNRs.[29] This defect can avoid introducing dangling bonds in the graphene lattice, thereby preserving lattice integrity. Previous studies have demonstrated that in ZGNRs containing 558 defects (denoted as ZGNR(558)), the carbon atoms at the center of the defect exhibit no magnetic moment.[30] Furthermore, the spins of its neighboring carbon atoms are aligned in an antiparallel configuration. As a result, ZGNR(558) maintains the intrinsic AFM ground state characteristic of pristine ZGNRs. Through the application of mechanical strain or elemental doping, a net magnetic moment

Department of Optical Engineering, College of Optical, Mechanical and Electrical Engineering, Zhejiang A&F University, Hangzhou, Zhejiang, 311300, P. R. China. E-mail: weiliu@zafu.edu.cn

can be induced at the defect-center carbon atoms.[31,32] This subsequently aligns the spins of the adjacent carbon atoms in a parallel manner, thereby leading to an AFM-to-ferromagnetic (FM) transition and rendering ZGNR(558) ferromagnetic.[30,33]

In this study, we employ density functional theory (DFT) to systematically incorporate 558 line defects into ZGNR/h-BN heterojunctions. This dual-engineering strategy combines defect engineering with heterojunction design to elucidate the cooperative modulation of electronic structure and magnetic order in ZGNRs. Our calculations reveal that the carbon atoms at the 558 defect center within the heterojunction still carry no magnetic moment; however, their neighboring carbon atoms intrinsically exhibit pronounced spin polarization with parallel alignment. This behavior drives a transition from AFM to FiM ordering in the ZGNR/h-BN heterojunction, concurrently endowing the system with half-metallic character. Furthermore, we systematically investigate the effects of ZGNR width, 558 defect position, and external strain on the electronic and magnetic properties of the heterojunction. These manipulations facilitate not only a FiM-to-FM transition but also yield various valuable spintronic features, such as half-semimetallicity coupled with high Fermi velocity. This work systematically demonstrates the unique capability of synergistic defect-heterojunction engineering in controlling magnetic transitions and enriching electronic properties.

2. Calculation method

First-principles calculations within the framework of density functional theory[34] were performed using the Vienna *Ab initio* Simulation Package (VASP).[35] The projector-augmented wave (PAW) method[36] was employed to describe ion–electron interactions. The exchange–correlation interactions were treated using the spin-polarized Perdew–Burke–Ernzerhof (PBE) functional within the generalized gradient approximation (GGA).[37] A plane-wave energy cutoff of 550 eV was used. The convergence criteria for the total energy were set to 10^{-5} eV per atom, and the force on each atom was relaxed to below 0.01 eV Å^{-1}. To avoid interactions between periodic images along the Z direction, a vacuum layer of 15–20 Å was applied. For Brillouin zone sampling, k-point meshes of $1 \times 4 \times 1$, $1 \times 8 \times 1$, and $1 \times 16 \times 1$ were used for structural relaxation, self-consistent field (SCF) calculations, and electronic property calculations, respectively.[38]

3. Results and discussion

3.1. ZGNR/hBN heterojunction with 558 defects

Fig. 1(a) illustrates the structure of a heterojunction formed by embedding a six-carbon-chain-wide ZGNR into a two-dimensional hexagonal boron nitride (h-BN) lattice, with the flanking h-BN regions consisting of five B–N chains on each side of the ZGNR. This structure is referred to as ZGNR/hBN-W, where "*W*" represents the width of the ZGNR. Specifically, Fig. 1(a) depicts the structure of ZGNR/hBN-6. Subsequently, a 558-type topological line defect, consisting of pentagons and octagons, is introduced into the center of the ZGNR, yielding the structure designated as ZGNR(558)/hBN-W. For ZGNR/hBN-6, this defect incorporation adds an extra carbon chain, resulting in the ZGNR(558)/hBN-7 configuration shown in Fig. 1(b). Both structures exhibit PMM2 symmetry and are fully planar after structural relaxation. The heterojunction width increases from 34.69 Å to 36.04 Å upon defect introduction. Notably, the introduction of the 558 defect causes some C–C bond lengths to elongate, while others contract, with the bond length range shifting from 1.43–1.44 Å to 1.40–1.47 Å. In contrast, B–N bond lengths remain consistent (1.44–1.45 Å) across both heterojunctions.

The formation energy was calculated to evaluate the effect of introducing the 558 defects on the thermodynamic stability of the ZGNR/hBN heterojunction. The formation energy (ΔE) is computed using the following formula:

$$\Delta E = (E_{\text{total}} - n_{\text{C}}E_{\text{C}} - n_{\text{BN}}E_{\text{BN}})/n_{\text{C}} + (2n_{\text{BN}})$$

where E_{total}, E_{C}, and E_{BN} represent the total energy of the heterojunction structure, the energy of one C atom from graphene, and the energy of a BN atom pair from h-BN sheet, respectively. n_{C} and n_{BN} represent the total number of C atoms and BN atom pairs. A lower formation energy indicates a stronger interface binding and greater structural stability. Calculation results (listed in Table S1) show that the formation energy of ZGNR(558)/hBN-7 (0.042 eV) is slightly lower than that of ZGNR/hBN-6 (0.047 eV), indicating that the heterojunction retains excellent thermodynamic stability despite the introduction of 558 topological defects.

The spin-polarized band structures and projected density of states (PDOS) for ZGNR/hBN-6 and ZGNR(558)/hBN-7 are shown in Fig. 1(c and d). For ZGNR/hBN-6, the spin degeneracy is lifted, yielding a Dirac half-metal: the spin-up channel is metallic (0 eV gap) while the spin-down channel is semiconducting with a direct bandgap of 0.03 eV, consistent with previous reports.[39,40] The spin-up dispersion forms a Dirac cone at the Fermi level with a Fermi velocity of 3.5×10^5 m s^{-1}, comparable to pristine graphene (1×10^6 m s^{-1}).[41–43] Upon the introduction of the 558 defects, ZGNR(558)/hBN-7 becomes a conventional half-metal: the spin-up channel is metallic, while the spin-down gap increases to 0.18 eV. As indicated by the insets in Fig. 1(c and d), carbon atoms of the ZGNRs are categorized as C1 (edge carbons), C2 (non-edge, non-defect carbons), and C3 (defect carbons). In ZGNR/hBN-6, the electronic states near the Fermi level in both spins are dominated by C1, with notable N contributions in the unoccupied spin-up states; C2 and B contribute negligibly near the Fermi level. In ZGNR(558)/hBN-7, the 558 defect introduces additional states around the Fermi level: for the spin-up channel, both occupied and unoccupied states are dominated by C1 and C3; for the spin-down channel, the occupied states are primarily C3-derived, whereas the unoccupied states are largely contributed by C1 and C3. Thus, the 558 defects introduce defect-localized states near the Fermi level, and enhances hybridization between edge (C1) and defect (C3) carbons, thereby reshaping the electronic structure and driving a transition from Dirac half-metallicity in ZGNR/hBN-6 to conventional half-metallicity in ZGNR(558)/hBN-7.

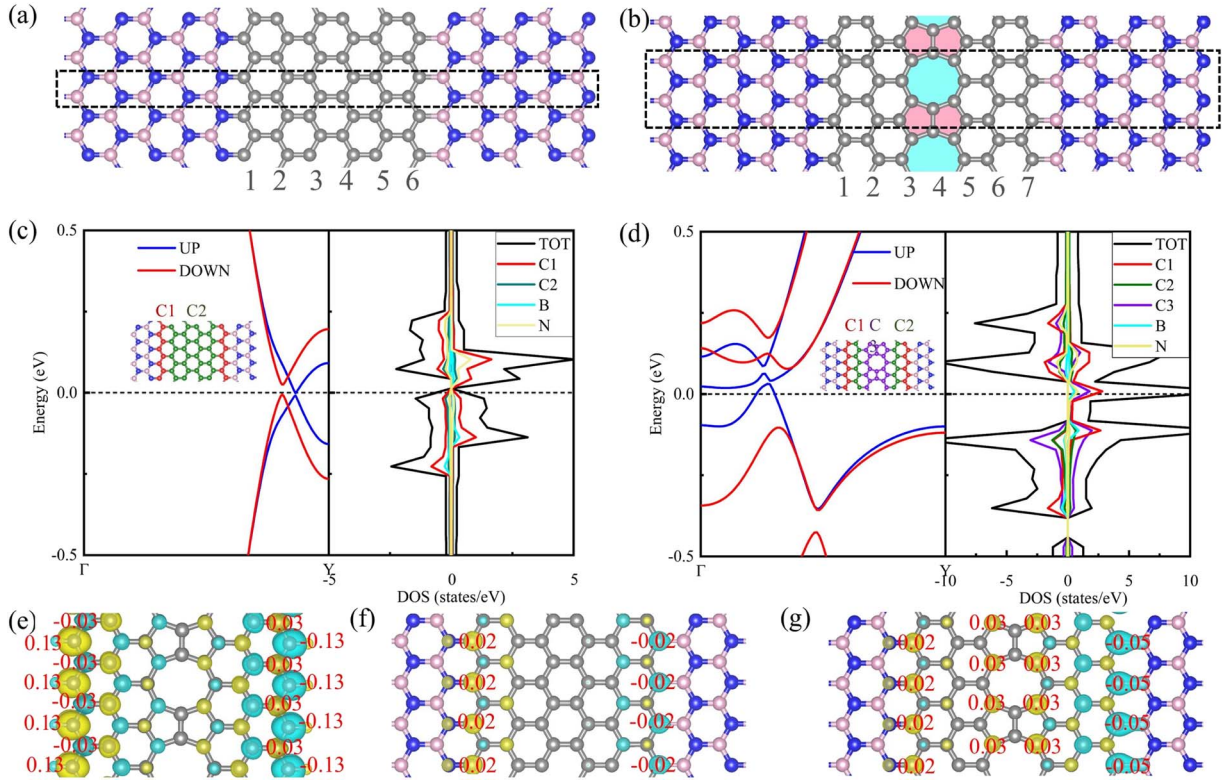

Fig. 1 (a and b) Atomic structures and (c and d) spin-polarized band structures with PDOS for ZGNR/hBN-6 and ZGNR(558)/hBN-7, respectively. (e–g) spin density distribution for ZGNR(558), ZGNR/hBN-6, and ZGNR(558)/hBN-7. Gray, blue, and magenta spheres denote C, N, and B atoms, respectively. Dashed rectangles mark the unit cells. In the band structures, blue and red curves correspond to spin-up and spin-down channels, and the Fermi level is set to 0 eV (dashed lines). Insets classify carbon atoms as C1 (edge, red), C2 (non-edge/non-defect, green), and C3 (defect, violet). The value of the isosurface level is 1×10^{-3} e Å^{-3}. Red numerical values indicate the calculated local magnetic moments (in μB) at the edge atoms and defect sites.

It is well-established that ZGNRs exhibit intrinsic AFM order. Previous studies confirm that introducing 558 defects at the central region of ZGNRs preserves the AFM behavior, with spin density primarily localized on the hydrogen-terminated edge carbon atoms and antiparallel spin alignment both at the edges and around the 558 defect center (Fig. 1(e)).[30] Specifically, the primary edge carbon atoms exhibit perfectly symmetric local magnetic moments of 0.13 μB and −0.13 μB. Similarly, embedding ZGNRs within an h-BN matrix to form the ZGNR/hBN-6 heterojunction yields an AFM ground state.[14] As shown in Fig. 1(f), the spin density remains concentrated on the edge carbon atoms interfacing with the h-BN regions. These opposite sides feature an antiparallel spin alignment with balanced local magnetic moments of 0.02 μB and −0.02 μB, while the central region shows negligible spin density. Notably, neither the individual introduction of 558 defects nor the construction of h-BN heterojunctions alters the AFM character of ZGNRs.

However, the application of a dual-engineering strategy by introducing 558 defects at the center of a ZGNR/hBN-6 heterojunction induces a critical transition. In the resulting ZGNR(558)/hBN-7 heterojunction, although the carbon atoms at the center of the 558 defect possess no net magnetic moment, the synergistic effect of the lattice distortion they induce and the h-BN interfacial environment reconstructs the electronic states of their neighboring carbon atoms. This synergy causes the spins of these neighboring carbon atoms to transition from an antiparallel (AFM) alignment in the isolated ZGNR(558) (Fig. 1(e)) to a parallel alignment with a local magnetic moment of 0.03 μB per atom (Fig. 1(g)). This defect-induced spin polarization reconstruction introduces a localized net magnetic moment in the central region, thereby breaking the global antiferromagnetic symmetry.

Simultaneously, the carbon atoms at the left and right edges of the ZGNR within the heterojunction are bonded to the N and B atoms of the h-BN lattice, respectively. They reside in distinct chemical environments due to the inherent difference between C–N and C–B bonds. This intrinsic edge asymmetry means that the aforementioned spin reconstruction affects the magnetic moments of the left and right edges to different extents. As demonstrated by the quantitative magnetic moment data (Fig. 1(g)), the carbon atoms at the *N*-terminated edge possess a magnetic moment of 0.02 μB per atom, whereas those at the B-terminated edge exhibit −0.05 μB per atom. This ultimately results in unequal total magnetic moments at the two boundaries. Therefore, the combined effect of the defect-driven spin reconstruction and the interfacial edge asymmetry unambiguously drive the system from a net-zero magnetic moment AFM ground state to a FiM ground state with a net magnetic

moment. Specifically, this spin-polarized behavior yields a total macroscopic magnetic moment of 0.0024 μB and an exchange energy of 1.83 meV. Together, these effects enable efficient modulation of the spin state in the graphene nanoribbons, permitting magnetic order switching even in the absence of external magnetic or electric fields.

3.2. ZGNR(558)/hBN-W heterojunctions with varying ZGNR widths

The electronic and magnetic properties of ZGNRs exhibit a strong and intricate dependence on their width. Therefore, to systematically investigate the influence of the ZGNR width on the structural stability, electronic and magnetic properties of ZGNR(558)/hBN-W heterojunctions, we constructed a series of heterostructures with varying ZGNR widths ($W = 5, 7, 9, 11, 13$). Their optimized structures are shown in Fig. 2(a) and S1. In these structures, the width of the h-BN regions on both sides is fixed at five BN chains, while the width of the central ZGNR region increases progressively from 5 to 13 carbon-chains. All optimized structures retain a fully planar configuration. As shown in Fig. 2(b), the formation energies of these heterojunctions range narrowly from 0.035 eV to 0.045 eV and display a distinct decreasing trend with increasing ZGNR width. Among them, the structure with the highest formation energy, ZGNR(558)/hBN-5, was selected for further validation through *ab initio* molecular dynamics (AIMD) simulation, which was performed at 500 K over 50 000 steps (50 ps) using a 1 × 4 supercell. As shown in Fig. S2, the results demonstrate that ZGNR(558)/hBN-5 retains its topological structure throughout the simulation, with the total energy oscillating near the equilibrium state, indicating excellent thermal stability.

The magnetic ground states of ZGNR(558)/hBN-W ($W = 5, 7, 9, 11, 13$) heterojunctions were determined by calculating their energies in various spin states. The results indicate that all structures exhibit ferrimagnetic ordering, except for ZGNR(558)/hBN-5, which is nonmagnetic. As W increases from 7 to 13, the exchange energy decreases from 1.83 meV to 0.03 meV, while the total magnetic moment increases from 0.0024 μB to 0.077 μB (summarized in Table S2). Their projected band structures and PDOS are presented in Fig. 3 and S3. It can be observed that both spin-up and spin-down electronic structures of ZGNR(558)/hBN-W exhibit a clear evolution with increasing ribbon width W. When $W = 5$, the system behaves as a nonmagnetic semiconductor with an indirect band gap of 0.15 eV. In the spin-up channel, the system exhibits metallic behavior at widths $W = 7$ and 9. While at larger widths ($W = 11$ and 13), Dirac cones emerge near the Fermi level with high Fermi velocities of 3×10^5 m s^{-1} and 2.6×10^5 m s^{-1}, respectively, indicating a transition to a semimetallic phase. This behavior originates primarily from the dominant contribution of C1 atoms to the electronic bands near the Fermi level. Fundamentally, the formation conditions of these Dirac cones are governed by the competition between finite-size quantum confinement and the spatial hybridization of local states. To elucidate this, we calculated the partial charge density near the Fermi level for varying widths (Fig. S4). In narrower nanoribbons ($W = 7$ and 9), the small spatial separation causes the localized wavefunctions of the edge states (C1) to overlap and hybridize with the central 558 defect states (C3) (Fig. S4(a and b)). This inter-state hybridization lifts the band degeneracy, thereby destroying the linear dispersion. Conversely, as the ribbon width increases, the wavefunctions decay exponentially. At larger widths ($W = 11$ and 13), the spatial distance becomes sufficient to effectively decouple the edge states from the defect states, as evidenced by the spatially separated and localized charge density distributions (Fig. S4(c and d)). This profound suppression of hybridization restores the band degeneracy at the Fermi level, identifying the critical factor that triggers the emergence of the Dirac cones in the spin-up channel. In the spin-down channel, the band gap decreases from 0.18 eV at $W = 7$ to 0.03 eV at $W = 11$, and eventually closes at $W = 13$, reflecting a transition from semiconductor to metal. Consequently, ZGNR(558)/hBN-W exhibits half-metallicity for $W = 7$ and 9; half-semimetallicity for $W = 11$; and metallic behavior for $W = 13$.

Fig. 4 shows the spin density distributions for ZGNR(558)/hBN-W ($W = 9, 11, 13$). The spin density is still primarily localized on the edge carbon atoms interfacing with the h-BN

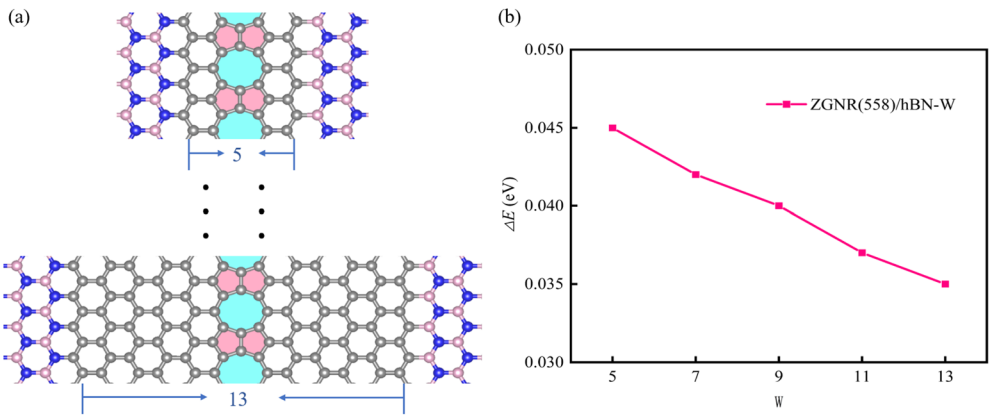

Fig. 2 (a) Schematic structures of ZGNR(558)/hBN-W ($W = 5, 7, 9, 11, 13$). (b) Formation energies of ZGNR(558)/hBN-W as a function of ZGNR width W.

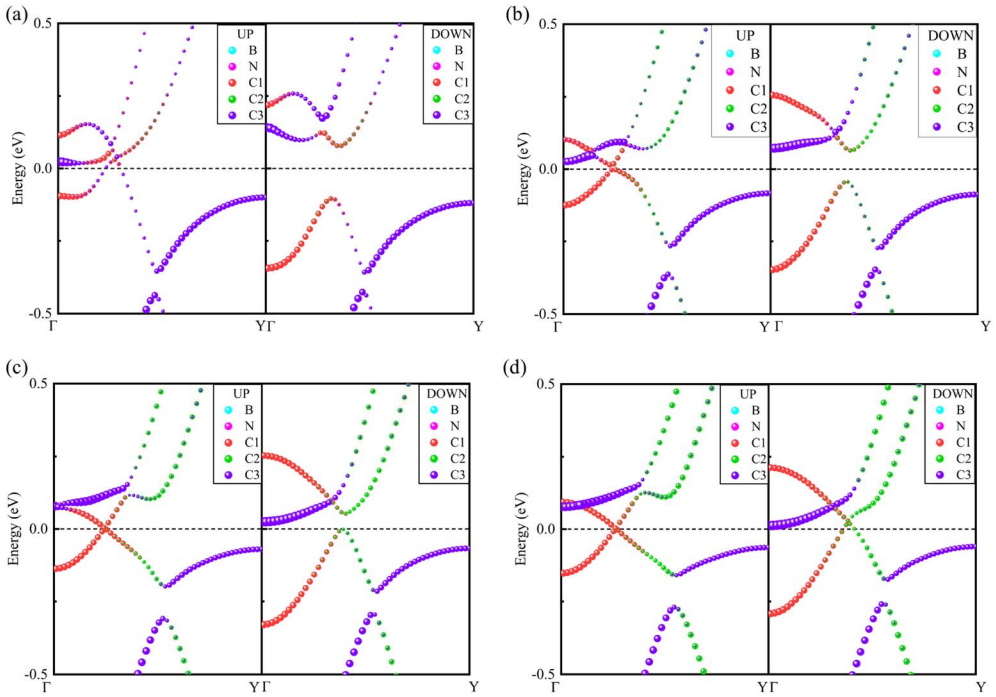

Fig. 3 Projected band structures of (a) ZGNR(558)/hBN-7, (b) ZGNR(558)/hBN-9, (c) ZGNR(558)/hBN-11, and (d) ZGNR(558)/hBN-13.

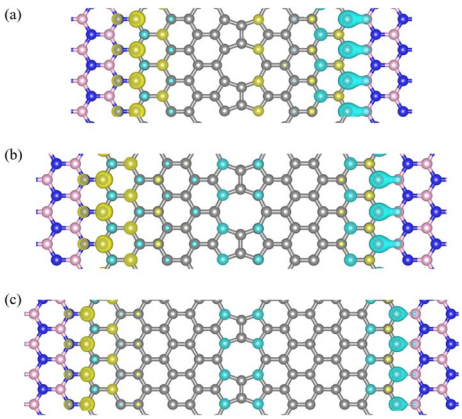

Fig. 4 Spin density distributions for (a) ZGNR(558)/hBN-9, (b) ZGNR(558)/hBN-11, and (c) ZGNR(558)/hBN-13. The value of the isosurface level is 1×10^{-3}e Å^{-3}.

regions and carbon atoms bonded to the central atoms of the 558 defects. As the ZGNR width W increases, the spin density distribution on edge carbon atoms remains relatively stable with minimal variation, maintaining antiparallel spin alignment on opposite sides. In contrast, the spin density in the defect region exhibits significant width dependence: at $W = 7$, the spin polarization direction of carbon atoms bonded to the central atoms of 558 defect is parallel alignment; at $W = 9$, the magnitude of this spin density markedly decreases; with further increase in width to $W = 11$ and 13, the spin polarization direction in the defect region undergoes a complete reversal. This phenomenon arises from the weakened quantum confinement effect at larger widths. In broader nanoribbons, the coupling between edge states diminishes, reducing their influence on the defect states. Consequently, the spin states in the defect region dominate the reconstruction of the local magnetic order. Simultaneously, the induced spin density on non-edge, non-defect carbon atoms (C2) systematically diminish with increasing W and becomes essentially negligible at $W = 13$.

3.3. ZGNR(558)/hBN-W heterojunctions with 558 defects at different positions

Prior studies have indicated that the properties of ZGNRs containing 558 defects are highly sensitive to the precise location of the defect. To elucidate the role of 558 defect positioning in ZGNR(558)/hBN heterojunctions, we systematically translated the defects along the armchair direction of ZGNR(558)/hBN-7. Defect positions were characterized by defining L and R as the number of carbon chains flanking the defect on the left and right sides, respectively, under the constraint $L + R = 4$. The resulting configurations are labeled as ZGNR(558)/hBN-7(LR). Fig. 5(a) shows the configurations for the leftmost ($L = 0$, $R = 4$) and rightmost ($L = 4$, $R = 0$) defect positions, while the other configurations are provided in Fig. S5. As summarized in Table S1, the calculated formation energy ΔE of these systems varies within a narrow range of only 0.039–0.043 eV as the defect shifts from the left to the right edge, indicating that the defect position has negligible impact on the energetic stability of the heterojunctions.

Energy calculations under different spin states reveal that ZGNR(558)/hBN-7(04) adopts an FM ground state, which is 4.42 meV more stable than the AFM state, and exhibits a magnetic moment of 0.50 μB. In contrast, all other structures exhibit

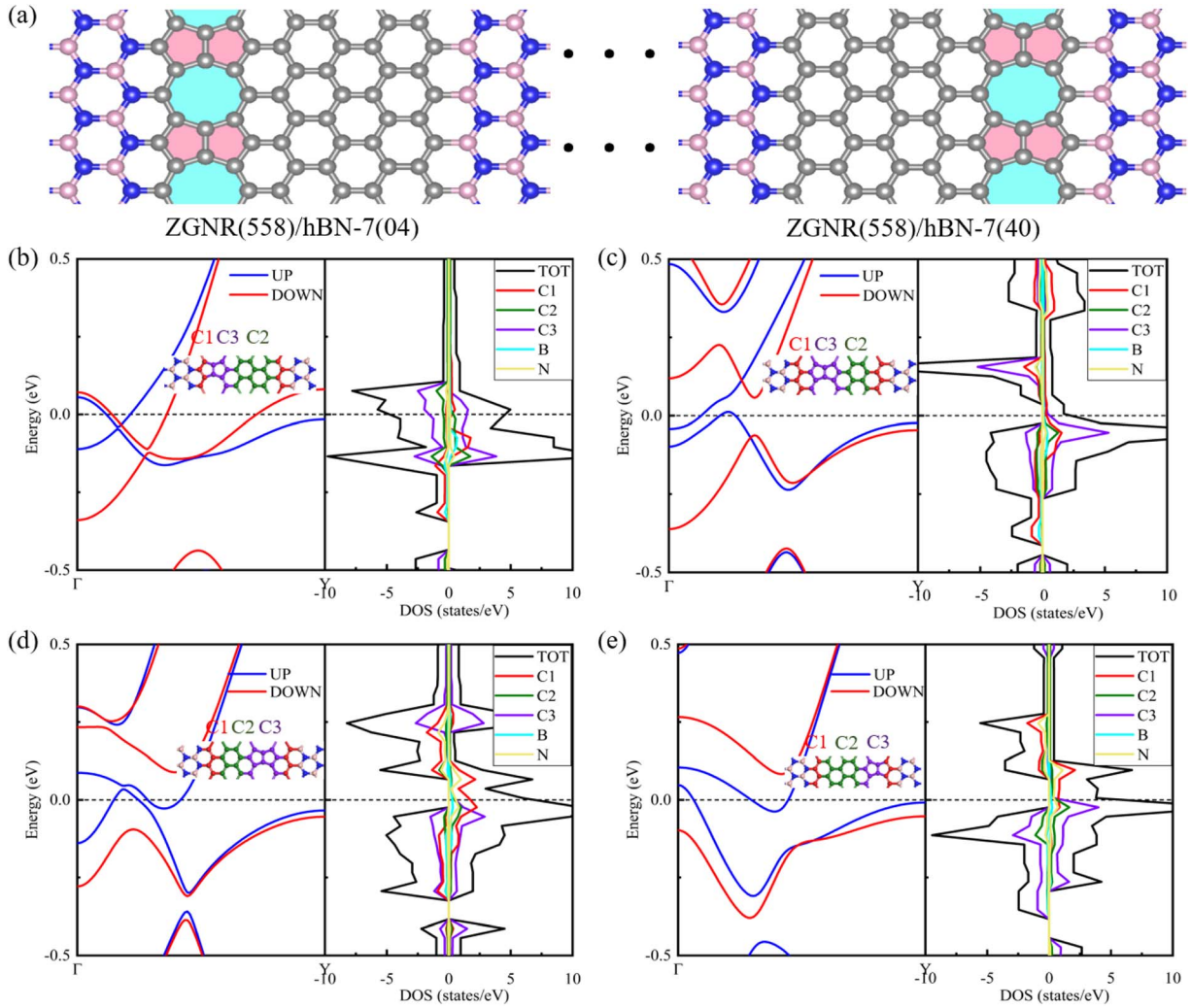

Fig. 5 (a) Schematic structures of ZGNR(558)/hBN-7(LR) with 558 defects at different positions. Band structures and PDOS for (b) ZGNR(558)/hBN-7(04), (c) ZGNR(558)/hBN-7(13), (d) ZGNR(558)/hBN-7(31), and (e) ZGNR(558)/hBN-7(40).

a ferrimagnetic ground state, with exchange energies ranging from 0.60 to 2.90 meV and total magnetic moments between 0.0024 and 0.012 μB. To investigate the microscopic origin of the FM state uniquely formed at the leftmost position (ZGNR(558)/hBN-7(04)), we have calculated both the charge density difference distributions and the interfacial C-to-N electron transfer using the Bader charge method for the heterojunctions with the defect at various positions. As confirmed by the charge density difference plots shown in Fig. S6, the direct defect-N connection in ZGNR(558)/hBN-7(04) induces a stronger interfacial charge redistribution. Quantitative Bader analysis corroborates this, revealing that the electron transfer from the carbon edge to the nitrogen atoms peaks at 0.52e for ZGNR(558)/hBN-7(04), which is substantially higher than the baseline of 0.40–0.45e observed in the other heterojunctions. This intensified electron depletion on the *N*-proximal carbon edge perfectly corroborates the diminished local spin density observed in Fig. 6(a). The elimination of these antiparallel spins breaks the global FiM balance of the nanoribbon, forcing the remaining spins at the central defect and the B-terminated edge to align parallelly, thereby driving the entire system into a macroscopic FM ground state.

As shown in Fig. 5(b–e), band structure calculations indicate that the position of the 558 defects significantly modulates the spin-polarized electronic properties of ZGNR(558)/hBN-7(LR).

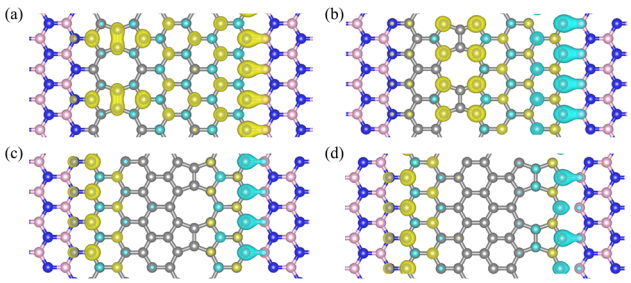

Fig. 6 Spin density distributions for (a) ZGNR(558)/hBN-7(04), (b) ZGNR(558)/hBN-7(13), (c) ZGNR(558)/hBN-7(31), and (d) ZGNR(558)/hBN-7(40).

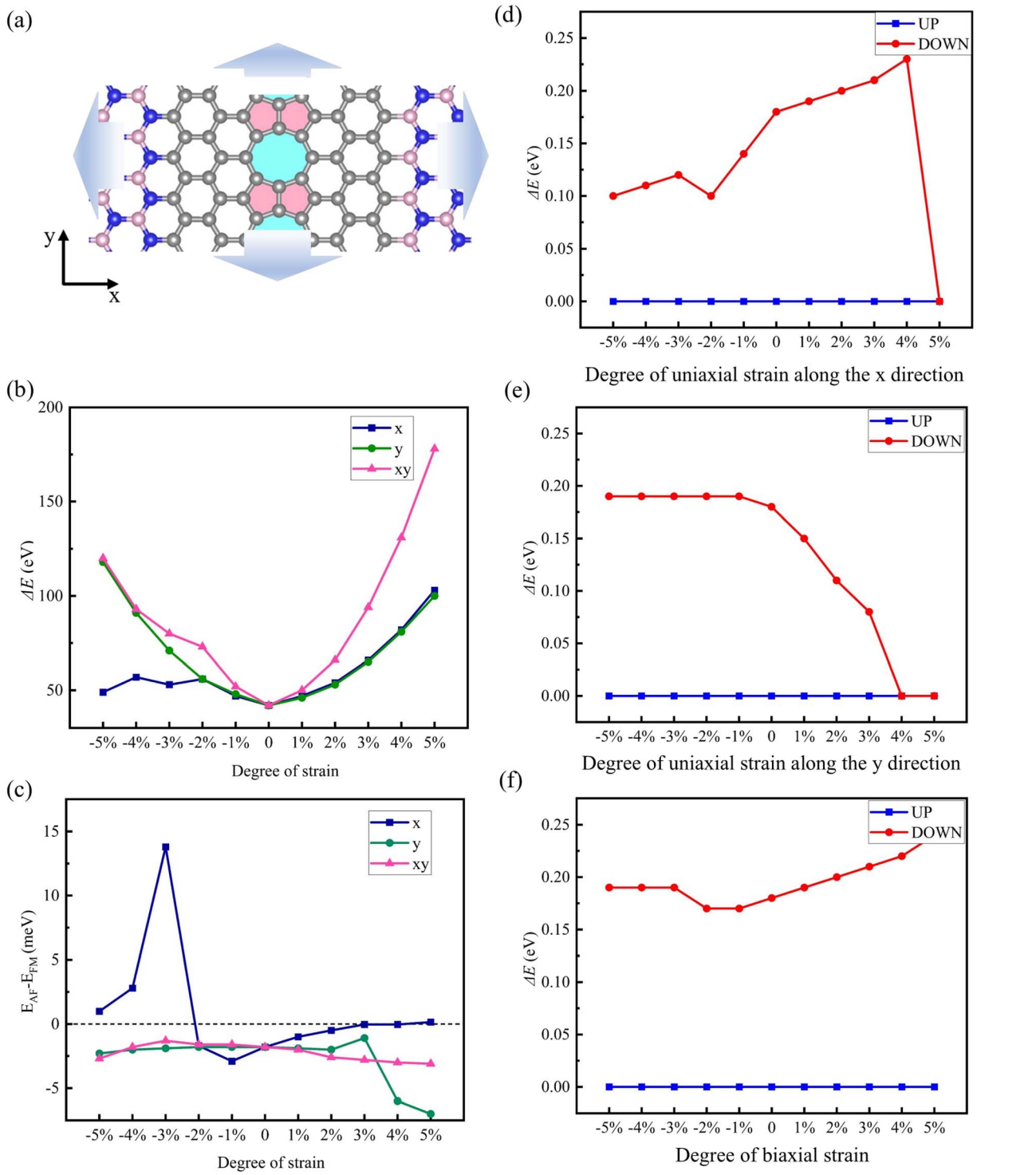

Fig. 7 (a) Schematic illustration of the application of uniaxial and biaxial strains on ZGNR(558)/hBN-7. Variation of (b) formation energy and (c) exchange energy under strain. Variation of the band gap for spin-up and spin-down channels under (d) uniaxial strain along the *x*-direction, (e) uniaxial strain along the *y*-direction, and (f) biaxial strain.

When the defect is located at the left edge ($L = 0$, $R = 4$), both spin-up and spin-down channels exhibit metallic behavior. As the defect shifts toward the right, the spin-up channel remains metallic, while the spin-down channel becomes semiconducting. The calculated spin-down gaps for configurations ZGNR(558)/hBN-7(13), (22) (31), and (40) are 0.10 eV, 0.18 eV, 0.15 eV, and 0.14 eV, respectively. The bandgap maximizes when the defect is centrally positioned and diminishes as it approaches either edge. To uncover the intrinsic mechanism driving the variation of the spin-down band gap with defect

position, we explicitly analyzed the defect-edge state energy level matching and wave function overlap (shown in Fig. S7 and S8). In the spin-down channel, the valence bands and conduction bands near the Fermi level are predominantly composed of the edge carbon states (C1) and the defect-center states (C3). When the defect is centrally located in ZGNR(558)/hBN-7(22), the large spatial separation effectively prevents the spatial overlap of wavefunctions between the defect and the edges (Fig. S8(d and e)). This spatial decoupling suppresses inter-state hybridization, allowing the system to maintain a maximum band gap of 0.18 eV. Conversely, shifting the defects toward either edge significantly enhances their structural proximity. Visually, the partial charge densities form a continuous distribution bridging the C3 and nearest C1 atoms (Fig. S8(b, c) and (h, i)), indicating strong wave function overlap. Simultaneously, the asymmetric interfacial potential shifts the C3 energy levels to resonate with the localized C1 states. This optimal energy matching, combined with the strong spatial overlap, triggers intense orbital hybridization. Consequently, the interacting bands disperse and shift toward the Fermi level, thereby systematically narrowing the spin-down band gap. These results demonstrate a viable route for tuning spin-resolved electronic properties in ZGNR-based heterostructures.

Fig. 6 depicts the spin density distributions of the ZGNR(558)/hBN-7(LR) heterostructures at varying defect positions. Overall, edge carbon atoms bonded to N and B retain antiparallel spin alignment. When the defects reside at the left edge, spin polarization on *N*-proximal edge carbon atoms is significantly suppressed. In contrast, discernible spin density emerges in this region only when the defect shifts toward the center or right edge. The spin density on *B*-proximal carbon atoms, however, remains largely unaffected by defect repositioning. Furthermore, displacing the defect rightward substantially reduces spin polarization on defect-associated carbon atoms.

3.4. ZGNR(558)/hBN-W heterojunctions under variable strains

Finally, the influence of strain on the properties of the ZGNR(558)/hBN-7 heterostructure was systematically investigated. As illustrated in Fig. 7(a), uniaxial strains ranging from ~5% to 5% were applied independently along the *x*- and *y*-directions, alongside biaxial strains within the same range. Fig. 7(b) shows that the formation energy of ZGNR(558)/hBN-7 increases slightly under both compression and tension, suggesting a mild decrease in energetic stability. The most significant change occurs under 5% biaxial tensile strain, where the formation energy increases from 0.042 eV to 0.18 eV. The variation of the exchange energy with strain is presented in Fig. 7(c). A transition from FiM to FM ordering is observed under 5% tensile strain or under compressive strain exceeding 3% along the *x*-direction, accompanied by a magnetic moment of 0.12–0.38 μB. Notably, at 3% compressive strain, the exchange energy reaches 13.83 meV, a value sufficient to stabilize magnetic order at room temperature. Under all other strain conditions, the system remains ferrimagnetic.

Fig. 7(d–f) depict the evolution of the bandgap for both spin channels in the ZGNR(558)/hBN-7 heterojunction under various strain conditions, with corresponding band structures provided in Fig. S9–S11. Overall, the half-metallic character is largely preserved across a wide range of strain regimes. A transition to metallic behavior occurs only under significant uniaxial tensile strain. Specifically, as illustrated in Fig. 7(d), uniaxial strain along the *x*-direction preserves metallicity in the spin-up channel, while the spin-down channel becomes metallic at 5% tensile strain. Under *y*-directional uniaxial strain (Fig. 7(e)), the spin-up channel remains metallic, whereas the spin-down band gap narrows under expansion and closes at 4% strain, resulting in full metallicity. Conversely, the heterojunction maintains half-metallicity across all examined biaxial strains (Fig. 7(f)).

4. Conclusion

In conclusion, we demonstrate a defect-engineering strategy utilizing first-principles calculations to achieve field-free control of magnetic and electronic states in ZGNR/h-BN heterojunctions. By introducing 558 topological line defects, we observe a spontaneous transition from the pristine AFM order to a FiM ground state, originating from reconstructed spin polarization at defect sites and asymmetric edge moments. Width-dependent studies reveal programmable electronic phase transitions. At $W = 7$, the system acts as a conventional half-metal, featuring a metallic spin-up channel and a spin-down band gap of 0.18 eV. With increasing ribbon width, the system evolves into a half-semimetallic phase at $W = 9$ and 11, characterized by Dirac cones with high Fermi velocities in the spin-up channel and progressively reduced spin-down band gaps. Finally, at $W = 13$, the system transitions to a fully metallic state. The positioning of defects along the nanoribbon axis can serve as a dual-functional switch for regulating both magnetic and electronic properties: by shifting the 558 topological defect, continuous modulation of the band gap in the spin-down channel within the range of 0 to 0.18 eV is achieved (the band gap reaches its maximum when the defect is centered), while a ferromagnetic ordered state with a magnetic moment of 0.50 μB is induced when the defect approaches the *N*-terminated edge. Additionally, the FiM state exhibits exceptional robustness under ±5% biaxial strain, maintaining half-metallicity, although uniaxial strain triggers transitions to ferromagnetic ordering under specific conditions (5% tensile strain or compressive strains exceeding 3% along the *x*-direction). This multi-field tunability, combining defect engineering with heterojunction design, establishes a platform for low-power spintronic devices, enabling efficient magnetic and electronic property manipulation without external fields.

Author contributions

W. L. and G. S. conceived the research; G. S. and W. L. performed the calculations and analyzed the data; W. L., G. S. and W. C. wrote the manuscript. All authors discussed and commented on the manuscript.

Conflicts of interest

The authors declare no competing financial or nonfinancial interests.

Data availability

The data supporting this article have been included as part of the supplementary information (SI). Supplementary information: schematic diagrams of the relevant heterostructures, additional electronic structures, the AIMD simulation results for thermal stability, and specific structural parameters used for VASP calculations. See DOI: https://doi.org/10.1039/d6ra01402j.

Acknowledgements

The publication of this article was supported by the author's personal resources.

References

1 X. Li and J. Yang, *Natl. Sci. Rev.*, 2016, **3**, 365–381.
2 Q. Sun, Y. Dai, Y. Ma, W. Wei, L. Yu and B. Huang, *Sci. Rep.*, 2015, **5**, 12772.
3 W. Han, K. M. McCreary, K. Pi, W. H. Wang, Y. Li, H. Wen, J. R. Chen and R. K. Kawakami, *J. Magn. Magn. Mater.*, 2012, **324**, 369–381.
4 S. A. Wolf, D. D. Awschalom, R. A. Buhrman, J. M. Daughton, S. von Molnár, M. L. Roukes, A. Y. Chtchelkanova and D. M. Treger, *Science*, 2001, **294**, 1488–1495.
5 D. Guo, X.-Y. Rui, S. Du, Q.-R. Liang, H. Yang and S.-J. Zheng, *Rare Met.*, 2025, **44**, 9336–9362.
6 S. Lou, B. Lyu, X. Zhou, P. Shen, J. Chen and Z. Shi, *Quantum Front.*, 2024, **3**, 3.
7 S. Song, Y. Teng, W. Tang, Z. Xu, Y. He, J. Ruan, T. Kojima, W. Hu, F. J. Giessibl, H. Sakaguchi, S. G. Louie and J. Lu, *Nature*, 2025, **637**, 580–586.
8 C.-M. Miao, Q.-F. Sun and Y.-T. Zhang, *Phys. Rev. B*, 2022, **106**, 165422.
9 Z. Qiao, S. A. Yang, B. Wang, Y. Yao and Q. Niu, *Phys. Rev. B:Condens. Matter Mater. Phys.*, 2011, **84**, 035431.
10 M. Pizzochero and E. Kaxiras, *Nano Lett.*, 2022, **22**, 1922–1928.
11 P. P. Shinde, O. Gröning, S. Wang, P. Ruffieux, C. A. Pignedoli, R. Fasel and D. Passerone, *Carbon*, 2017, **124**, 123–132.
12 Y. Cheng, J. Xu, J. Xiang, W. Liu and M. Miao, *Phys. Rev. B*, 2024, **110**, 085141.
13 C. Jiang, H. S. Wang, C. Liu, C. Chen, L. Chen, X. Wang, Y. Wang, Z. Kong, Y. Feng, Y. Liu, Y. Feng, Y. Zhang, Z. Wei, M. Guo, A. Tong, G. Mu, Y. Yang, K. Watanabe, T. Taniguchi, W. Shi and H. Wang, *Nat. Mater.*, 2025, **24**, 1592–1599.
14 N. V. Tepliakov, R. Ma, J. Lischner, E. Kaxiras, A. A. Mostofi and M. Pizzochero, *Nano Lett.*, 2023, **23**, 6698–6704.
15 J. Pan, W. Wei, Z. Gong and Y. Cui, *Carbon*, 2021, **177**, 19–25.
16 M. Wang, X. Li, Y. Li, X. Zuo, D. Li, B. Cui and D.-S. Liu, *Org. Electron.*, 2018, **58**, 63–68.
17 M. Pizzochero, N. V. Tepliakov, J. Lischner, A. A. Mostofi and E. Kaxiras, *Nano Lett.*, 2024, **24**, 6521–6528.
18 S. Cao, R. Zheng, C. Wang, N. Ma, M. Chen, Y. Song, Y. Feng, T. Hao, Y. Zhang, Y. Wang, P. Gu, K. Watanabe, T. Taniguchi, Y. Liu, X. C. Xie, W. Ji, Y. Ye, Z. Han and J.-H. Chen, *Adv. Mater.*, 2025, **37**, e2411300.
19 Y. Fei, Y. Fu, X. Bai, L. Du, Z. Li, H. Komber, K.-H. Low, S. Zhou, D. L. Phillips, X. Feng and J. Liu, *J. Am. Chem. Soc.*, 2021, **143**, 2353–2360.
20 Y. Ge, J. Ji, Z. Shen, Q. Zhang, A. Jian, Q. Duan, C. Wang, J. Jiang, W. Zhang and S. Sang, *Carbon*, 2018, **127**, 432–436.
21 J. Lu, Y. Bao, C. L. Su and K. P. Loh, *ACS Nano*, 2013, **7**, 8350–8357.
22 H. Deng, Z. Qu, Y. He, C. Huang, N. C. Panoiu and F. Ye, *Quantum Front.*, 2023, **2**, 11.
23 W. Liu, Y. Xie, L. Chen, M. Guo and J. Xu, *Mater. Today Sustain.*, 2024, **26**, 100699.
24 Y.-W. Liu and L. He, *Quantum Front.*, 2023, **2**, 2.
25 S. Mishra, D. Beyer, R. Berger, J. Liu, O. Gröning, J. I. Urgel, K. Müllen, P. Ruffieux, X. Feng and R. Fasel, *J. Am. Chem. Soc.*, 2020, **142**, 1147–1152.
26 H. Abdelsalam, D. Corona, R. B. Payod, M. A. S. Sakr, O. H. Abd-Elkader, Q. Zhang and V. A. Saroka, *Nano Lett.*, 2025, **25**, 10594–10602.
27 N.-J. Yang, W.-T. Guo, H. Yang, Z. Huang and J.-M. Zhang, *Phys. Chem. Chem. Phys.*, 2024, **26**, 17075–17082.
28 W. Lu, D. Zheng, D. Ye, J. Peng, X. Gong, J. Xu and W. Liu, *J. Mater. Inf.*, 2024, **4**, 31.
29 J. Lahiri, Y. Lin, P. Bozkurt, I. I. Oleynik and M. Batzill, *Nat. Nanotechnol.*, 2010, **5**, 326–329.
30 M. Kan, J. Zhou, Q. Sun, Q. Wang, Y. Kawazoe and P. Jena, *Phys. Rev. B*, 2012, **85**, 155450.
31 L.-H. Qu, J.-M. Zhang, K.-W. Xu and V. Ji, *Physica E*, 2015, **67**, 116–120.
32 Q. Q. Dai, Y. F. Zhu and Q. Jiang, *J. Phys. Chem. C*, 2013, **117**, 4791–4799.
33 X. Lin and J. Ni, *Phys. Rev. B:Condens. Matter Mater. Phys.*, 2011, **84**, 075461.
34 W. Kohn and L. J. Sham, *Phys. Rev.*, 1965, **140**, A1133–A1138.
35 G. Kresse and J. Furthmüller, *Phys. Rev. B:Condens. Matter Mater. Phys.*, 1996, **54**, 11169–11186.
36 G. Kresse and D. Joubert, *Phys. Rev. B:Condens. Matter Mater. Phys.*, 1999, **59**, 1758–1775.
37 J. P. Perdew, K. Burke and M. Ernzerhof, *Phys. Rev. Lett.*, 1996, **77**, 3865–3868.
38 H. J. Monkhorst and J. D. Pack, *Phys. Rev. B*, 1976, **13**, 5188–5192.
39 Y. Ding, Y. Wang and J. Ni, *Appl. Phys. Lett.*, 2009, **95**, 123105.
40 C. Leon, M. Costa, L. Chico and A. Latgé, *Sci. Rep.*, 2019, **9**, 3508.
41 J. R. F. Lima, *Phys. Lett. A*, 2015, **379**, 179–182.
42 C. Hwang, D. A. Siegel, S.-K. Mo, W. Regan, A. Ismach, Y. Zhang, A. Zettl and A. Lanzara, *Sci. Rep.*, 2012, **2**, 590.
43 A. R. S. Lins and J. R. F. Lima, *Carbon*, 2020, **160**, 353–360.